First Draft Manuscript: November 26, 2024

The Runoff Potential Index: Upland–Lowland Differentiation

V 1.0.0 (43 MB) – *Edgar Steven Correa*
[MATLAB Central File Exchange: The Runoff Potential Index – Upland–Lowland Differentiation]

MATLAB toolbox for 3D physics-based surface runoff simulation in low-slope agricultural landscapes. Supports terrain-driven drought vulnerability assessment via a curvature-based Runoff Potential Index (RPI). Updated June 11, 2025

Runoff potential index for upland-lowland drought assessment in rainfed rice using earth observation and mechanistic crop modelling

Edgar S. Correa[1,2,3*]

[1]Pontificia Universidad Javeriana, School of Engineering, Bogota Cra. 7 No. 40-62, 110311 Bogota, Colombia
[2]UMR AGAP Institut, Univ. Montpellier, CIRAD, INRAE, Institut Agro, Montpellier, France (2024)
[3]CIRAD, UMR AGAP Institut, F-34398, Montpellier, France (2024)
[*]e_correa@javeriana.edu.co

ABSTRACT

Drought vulnerability assessment in agricultural systems remains increasingly critical under climate change, yet current approaches are constrained by limitations of existing topographic indices, particularly in low-gradient terrains where the widely-used Topographic Wetness Index (TWI) exhibits numerical instability and fails to detect critical microtopographic variations that control water retention at field scales.

This study introduces the Runoff Potential Index (RPI), a curvature-based terrain metric that addresses specific limitations of slope-dependent indices for climate-resilient agricultural drought assessment: RPI$(x,y) = \nabla^2 z/(|\nabla z| + \varepsilon)$, integrating local terrain curvature (via Laplacian of elevation) with slope magnitude. The analysis presents complementary approaches combining: (1) RPI terrain analysis using satellite-derived elevation data for upland-lowland differentiation based on terrain-controlled water redistribution, identifying runoff-prone uplands versus water-retaining lowlands, and (2) CERES-Rice mechanistic crop modeling driven entirely by Earth observation data to evaluate drought stress patterns across varying sowing dates, supporting climate adaptation strategies in data-scarce regions.

The RPI maintained analytical sensitivity across subtle elevation gradients (0.7-1.8 m variations) where TWI becomes numerically unstable, successfully detecting centimeter-scale microtopographic variations critical for water retention. Terrain analysis revealed distinct upland-lowland differentiation patterns, with lowland areas achieving 200 kg/ha higher yields compared to upland areas. CERES-Rice simulations across 20 years (2000-2019) identified optimal sowing windows that minimize drought stress, with delayed sowing causing yield reductions exceeding 1,500 kg/ha. Critically, terrain-based yield advantages (200-300 kg/ha) are substantially smaller than temporal optimization benefits, exposing limitations in current mechanistic models that fail to adequately represent topographic water redistribution effects captured by RPI analysis.

The Earth observation-based framework enables drought vulnerability mapping without ground-based data requirements, supporting climate adaptation in agricultural systems globally. The findings reveal conceptual limitations in bucket-based crop models and demonstrate scalable approaches for drought-resilient agriculture under changing climate conditions. This framework enables practical climate adaptation through: (1) field-specific sowing recommendations that prevent 45-73% yield losses from suboptimal timing, (2) identification of drought-vulnerable zones requiring targeted water management, and (3) satellite-based drought risk assessment accessible to smallholder farmers in data-scarce regions, directly supporting SDG 13.1 (strengthen resilience and adaptive capacity to climate-related hazards) and SDG 13.3 (improve education and capacity-building on climate change adaptation).

Keywords: biosystems modelling, drought vulnerability, earth observation, terrain analysis, crop modeling, remote sensing, climate adaptation, precision agriculture.

Introduction

Drought represents one of the most persistent and economically devastating natural hazards globally, having affected over 1.5 billion people since 2000 and causing economic losses of at least $124 billion from 1998-2017[1], with recent estimates indicating annual global costs now exceed $307 billion[2]. As climate variability intensifies under changing atmospheric conditions, the frequency and severity of drought events are projected to increase across multiple agricultural regions, necessitating more sophisticated and scalable approaches for risk assessment and early warning systems[3]. Current drought monitoring frameworks, while technologically advanced, exhibit critical limitations. They fail to integrate terrain-mediated hydrological processes with dynamic agricultural impacts, resulting in incomplete vulnerability assessments.

Rice (*Oryza sativa*), supporting billions of people across Asia, Africa, and Latin America, provides a particularly clear example of this vulnerability challenge[4–6]. Rainfed rice systems remain highly vulnerable to drought stress during sensitive phenological stages such as flowering and grain filling, causing severe yield losses in regions characterized by high interannual rainfall variability, poor water storage capacity, and limited irrigation access, particularly in semi-arid regions of West Africa where rainfed systems predominate[7–10]. While mechanistic crop models (MCMs) such as CERES-Rice have demonstrated capabilities in simulating genotype–environment–management interactions, their scalability remains constrained by sparse meteorological data and the absence of spatially explicit terrain analysis[11–14].

Contemporary drought analysis relies predominantly on meteorological indices and satellite-derived biophysical indicators that excel at detecting *when* and *where* drought occurs but systematically underestimate how landscape morphology determines hydrological redistribution patterns[15,16]. Existing methodologies fail to account for how terrain characteristics, particularly the spatial arrangement of convex upland forms versus concave lowland areas, fundamentally control surface water divergence and drought vulnerability at sub-regional scales. This morphological gap becomes critical when assessing agricultural drought impacts in topographically diverse rice-growing regions, where terrain-mediated water availability and crop physiological responses jointly determine yield outcomes.

Topographic analysis employs diverse methodological approaches, with documented applications utilizing up to 22 distinct topographic indices in hydrological systems[17] and comprehensive global datasets providing standardized suites of topographic variables for environmental modeling[18]. These indices are classified into primary metrics (elevation, slope, aspect) directly derived from digital elevation models, and secondary indices that combine multiple primary attributes to characterize specific landscape processes[19,20]. The most widely applied secondary indices include the Topographic Wetness Index (TWI)[21], slope length factor (LS)[22], specific catchment area (SCA)[19], and downslope distance gradient (DDG)[23]. While curvature-based approaches exist—including profile curvature (Kp), tangential curvature (Kt)[24], and Laplacian operators[25]—these have been predominantly developed for geomorphological channel extraction and drainage network delineation[26] rather than agricultural water retention analysis. Critically, no existing index integrates local curvature analysis with slope steepness specifically to quantify morphological propensity for water retention in low-gradient agricultural systems where microtopographic variations determine crop establishment success.

Here, I introduce an analytical framework that addresses this critical knowledge gap through two complementary analyses: (1) a novel terrain-derived metric, the Runoff Potential Index (RPI), that addresses specific limitations of existing topographic indices in agricultural systems by quantifying morphological propensity for water retention using Laplacian of elevation analysis, enabling identification of drought-vulnerable versus resilient zones in low-gradient terrains where traditional slope-based indices exhibit reduced sensitivity; and (2) dynamic crop modeling through CERES-Rice to simulate water balance dynamics and their influence on crop water stress patterns, enabling automated differentiation between drought-vulnerable upland areas and resilient lowland zones. As detailed in the following section, existing topographic indices like TWI exhibit limitations in low-gradient agricultural systems. The RPI addresses this gap by quantifying how landscape curvature controls water flow behavior: convex areas (ridges, hilltops) tend to shed water and experience higher drought stress, while concave areas (valleys, depressions) collect and retain water, providing drought resilience. This is captured through the formulation $\mathrm{RPI}(x,y) = \nabla^2 z/(|\nabla z| + \varepsilon)$, where ε is a small numerical regularization term that avoids singularities when $|\nabla z| \to 0$. The index provides intuitive interpretation: negative values indicate flow divergence (upland areas prone to runoff), while positive values represent flow convergence (lowland areas with water retention potential). This framework evaluates whether Earth observation-derived terrain analysis captures drought stress variability that traditional mechanistic crop models fail to represent, providing insights for model refinement strategies that incorporate morphologic-driven water retention patterns.

This approach integrates curvature-based terrain analysis for upland-lowland differentiation with dynamic crop response modeling, addressing the documented limitations of slope-dependent indices (such as TWI[21,27]) in low-gradient agricultural landscapes where microtopographic variations determine water retention patterns critical for crop establishment and drought resilience. This framework extends beyond crop systems to provide regional-scale terrain-based vulnerability mapping and generate field-scale management recommendations for optimizing rainfed rice productivity across diverse agricultural systems, directly addressing the growing demand for decision-support tools and adaptation strategies under changing climatic conditions.

State-of-the-Art in Agricultural Drought Assessment

Contemporary drought assessment has evolved into six principal methodological clusters, each addressing specific aspects of drought characterization but exhibiting critical limitations for comprehensive regional vulnerability analysis.

Meteorological approaches employ standardized indices such as the Standardized Precipitation Index (SPI) of McKee et al.[28], calculated as (Current Rainfall minus Long-Term Mean) divided by Rainfall Standard Deviation. Negative values indicate increasing drought severity. The Rainfall Anomaly Index (RAI) of Van Rooy[29] is defined as 3 times (Current Rainfall minus Average) divided by (Extreme Difference minus Average), highlighting how extreme a rainfall event is relative to historical extremes. These indices are operationally implemented by NASA's Global Drought Monitor and the European Drought Observatory using CHIRPS precipitation data processed in Google Earth Engine.

Biophysical methods integrate vegetation and soil response indicators such as the Vegetation Condition Index (VCI) of Kogan[30], computed as 100 times (NDVI minus Minimum NDVI) divided by (Maximum NDVI minus Minimum NDVI); values below 40 indicate severe vegetation stress. The Temperature Condition Index (TCI)[31] is calculated as 100 times (Maximum Temperature minus Actual Temperature) divided by (Maximum Temperature minus Minimum Temperature) to detect heat stress. The Microwave Water Stress Index (MWSI) of Zhang and Jia[32] is given by (Horizontal Brightness Temperature minus Vertical Brightness Temperature) divided by their sum, capturing canopy water stress from microwave emissions. Topographic analysis commonly uses the Topographic Wetness Index (TWI) of Beven and Kirkby[21, 27] and the Terrain Ruggedness Index (TRI) of Riley et al.[33], calculated as the sum of elevation differences between each neighboring cell and the central cell divided by the number of cells. These indicators are implemented by NOAA/NESDIS, FAO GIEWS, and USDA GLAM using MODIS, Sentinel-3, and SMAP data, but they address isolated terrain aspects without fully integrating how morphology redistributes water.

Spatial enhancement techniques developed by major technology companies focus primarily on improving resolution rather than resolving underlying process uncertainties. The NOAA Climate Prediction Center applies the PRISM method[34], where precipitation is estimated as Base Value plus Elevation times Factor plus Slope times Factor plus Aspect times Factor plus Distance to Ocean times Factor. Google AI and DeepMind refine local temperature estimates using lapse rates that adapt dynamically: Temperature equals Base Temperature minus Elevation times Cooling Rate, with the cooling rate learned from local conditions. Microsoft AI for Earth operationalizes these algorithms on Azure Cloud to produce 10-meter drought products, while Copernicus C3S uses advanced multisensor fusion combining Sentinel-1, Sentinel-2, and Sentinel-3 data.

Critical threshold detection uses indices such as the Palmer Drought Severity Index (PDSI)[35], computed as 0.897 times the previous month value plus Current Moisture Index divided by 3; values below -3 indicate severe drought and are monitored by the U.S. Drought Monitor. The Modified Normalized Difference Water Index (MNDWI)[36] is defined as (Green Band minus Infrared Band) divided by their sum, where negative values indicate the absence of surface water. The Surface Energy Balance Algorithm for Land (SEBAL)[37] estimates actual evapotranspiration as (Net Radiation minus Soil Heat Flux minus Sensible Heat Flux) divided by the Latent Heat of Vaporization. This is implemented operationally in ERA5-Land by ECMWF with hourly resolution.

Conceptual hydrological modeling uses interconnected tank systems to simulate runoff generation and water storage processes. Classical models include Ishihara-Kobatake[38] with three cascade tanks, the Japanese NRCDP Tank model[39] for river flow prediction, the Swedish HBV Tank[40] with snowmelt routines, the Sacramento model[41] used by the National Weather Service, TOPMODEL Tank[21] based on topographic indices, the Danish NAM[42], and the Australian AWBM[43]. Additionally, crop models such as CERES-Rice in the DSSAT system[44] apply a tank-based water balance to simulate evapotranspiration and crop physiological response. These models remain widely adopted in R packages like `airGR`, `TUWmodel`, and `hydromad`, valued for conceptual simplicity, computational efficiency, and real-time forecasting, with increasing integration into machine learning frameworks and early warning systems.

Machine learning automation applies Random Forest classifiers[45] developed by Google Research, Support Vector Machines by Microsoft Research, and ensemble methods by Amazon Web Services, achieving validation accuracies up to 95% for drought classification.

Despite significant progress across all methodological clusters, a critical challenge persists: the lack of physically-based quantification of how landscape morphology controls hydrological redistribution at agricultural scales. Existing approaches excel in monitoring precipitation deficits, biophysical stress, and threshold detection, yet systematically overlook how terrain determines where water accumulates and persists. Widely used indices like TWI become unstable in low-gradient croplands and fail to resolve subtle microtopographic depressions that critically influence field-level water retention and crop survival during drought. This limitation highlights opportunities for terrain-derived metrics that integrate local curvature, slope, and microrelief analysis, enabling predictive drought vulnerability assessment based on inherent landscape structure rather than relying solely on reactive monitoring approaches.

This paper presents a comprehensive framework combining terrain analysis with mechanistic crop modeling for agricultural drought vulnerability assessment. This approach describes the development and implementation of the Runoff Potential Index using satellite-derived elevation data, alongside the parameterization of CERES-Rice crop models driven entirely by Earth observation datasets including SoilGrids and NASA POWER meteorological data. The analysis evaluates RPI performance against conventional topographic indices across synthetic terrain scenarios, demonstrates regional-scale upland-lowland differentiation mapping across West African agricultural landscapes, and presents 20-year drought stress simulations to identify optimal sowing strategies. The study concludes with a critical comparison between terrain-based predictions and mechanistic crop model outputs, revealing structural limitations in current bucket-based water balance approaches and highlighting opportunities for integrating topographic water redistribution processes into agricultural modeling frameworks. This integrated approach provides both methodological advances for drought assessment and practical tools for climate adaptation in rainfed agricultural systems.

Results

Comprehensive evaluation of RPI analytical performance versus TWI

To evaluate RPI analytical performance against the widely used Topographic Wetness Index (TWI), comparative analysis was conducted using synthetic terrain scenarios spanning four distinct morphological zones. Figure 1 presents quantitative performance comparison between TWI and RPI across a 1 km × 1 km synthetic field at 2.5 m spatial resolution, with seven representative measurement points providing precise coordinate-based validation across concave depressions, convex elevations, subtle undulations, and flat reference terrain.

Zone 1 analysis reveals fundamental differences in index sensitivity. Across the concave depression with a 1.8 m elevation difference, with RPI values ranging from 1.359 at the crater minimum (98.015m elevation) to -0.013 at the crater boundary (99.853m elevation). TWI produces remarkably similar values of 23.305 and 23.126 at these morphologically distinct locations. Zone 2 (convex mountain) shows RPI values of -1.359 at the mountain maximum (101.985m elevation) and 0.013 at the mountain curvature (100.149m elevation), with corresponding TWI values of 14.433 and 23.254. Zone 3 (low-amplitude undulations) exhibits microtopographic variations of 70 cm elevation difference between wave maximum (100.606m) and wave minimum (99.902m), with corresponding RPI values of 2.496 and -1.708, while TWI yields considerably higher values of 23.727 and 16.811. Notably, at the flat reference point (100.000m elevation), RPI exhibits 0.000 while TWI reaches 48.660—a value even higher than those observed in topographically complex zones, demonstrating fundamental numerical instability.

Critical evaluation emerges in the morphological transition zones where RPI demonstrates superior sensitivity to subtle terrain changes. At the crater curvature boundary (P2), RPI exhibits -0.013, correctly identifying the transition from water-retentive to neutral conditions, while at the mountain curvature (P4), RPI shows +0.013, indicating the opposite transition from runoff-prone to neutral terrain. This demonstrates RPI's capacity to detect directional morphological transitions with opposite physical meanings. Conversely, TWI produces nearly identical values at these transition points (23.126 vs 23.254), failing to distinguish between morphologically driven concentrates or disperses water flow patterns.

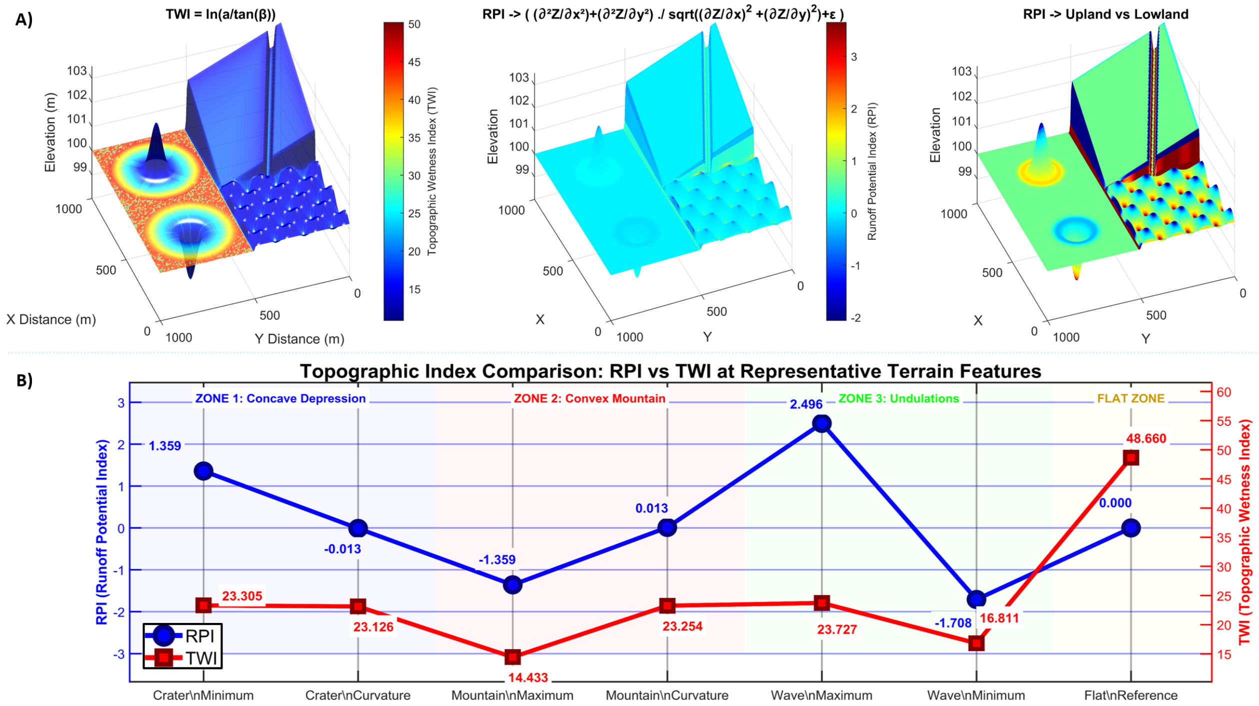

Figure 1. Comparative analysis of topographic indices across diverse terrain conditions. (A) Three-dimensional visualizations: TWI (left) exhibits numerical instability in flat areas (red regions show extreme values approaching 50), RPI (center) maintains stability across all terrain types (range: -2 to +3), and RPI-based terrain classification (right) identifying upland areas (percentiles <0.2, blue) and lowland areas (percentiles >0.8, red). (B) Quantitative comparison at seven representative points across four terrain zones. RPI (blue line) demonstrates consistent physical interpretation: negative values indicate runoff-prone upland areas, positive values indicate water-retaining lowland areas. TWI (red line) produces nearly identical values at morphologically opposite transition points (23.126 vs 23.254), failing to distinguish between terrain features that control contrasting water flow patterns.

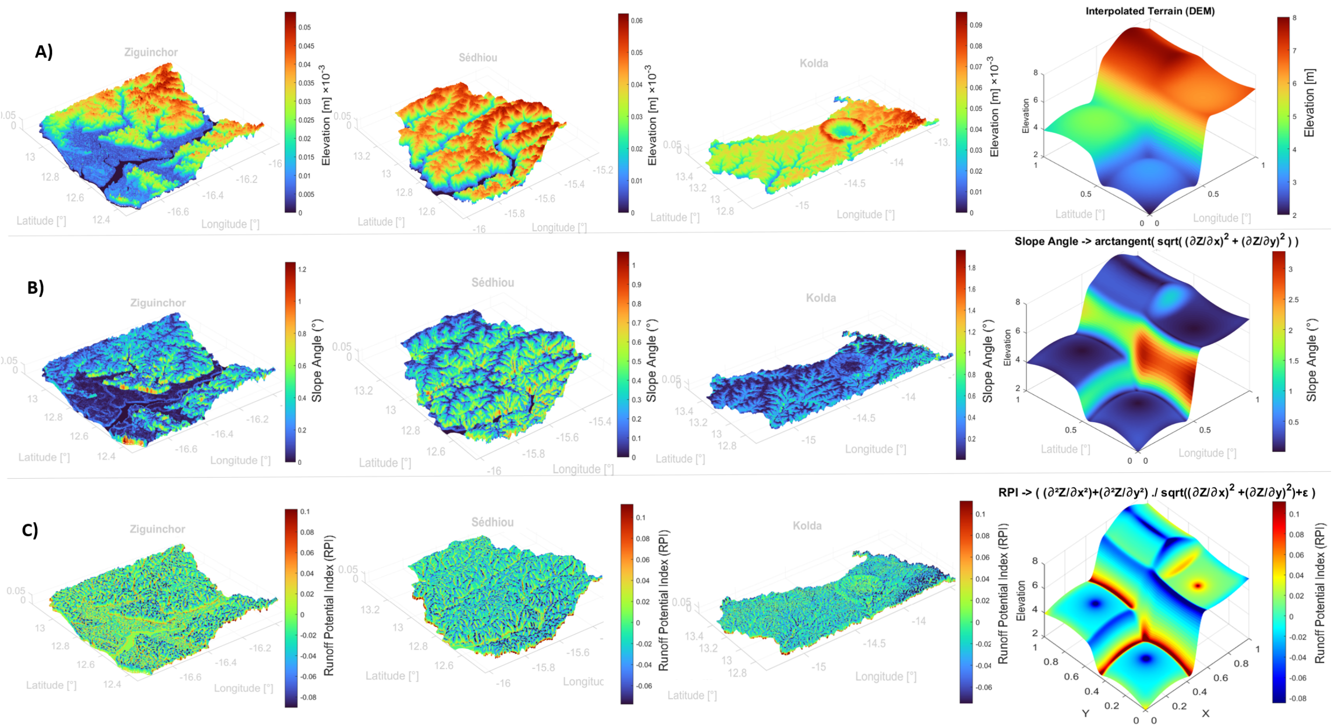

Figure 2. Comparative terrain analysis across three agricultural regions with reference demonstration. (A) Digital elevation models showing topographic variation across the study areas, with 3D visualization (right panel); (B) Slope angle distributions highlighting terrain steepness gradients; (C) Runoff Potential Index (RPI) integrating curvature and slope to quantify water redistribution potential. Negative RPI values (blue) indicate runoff-prone upland areas, while positive values (red) indicate water-retaining lowland areas. The rightmost column provides a reference demonstration of RPI behavior across controlled terrain conditions.

Satellite-based terrain analysis and runoff potential

Satellite-based remote sensing provides high-resolution elevation data suitable for geomorphological terrain-based water divergence mapping. Figure 2 demonstrates the analytical framework applied across three agricultural regions, with an

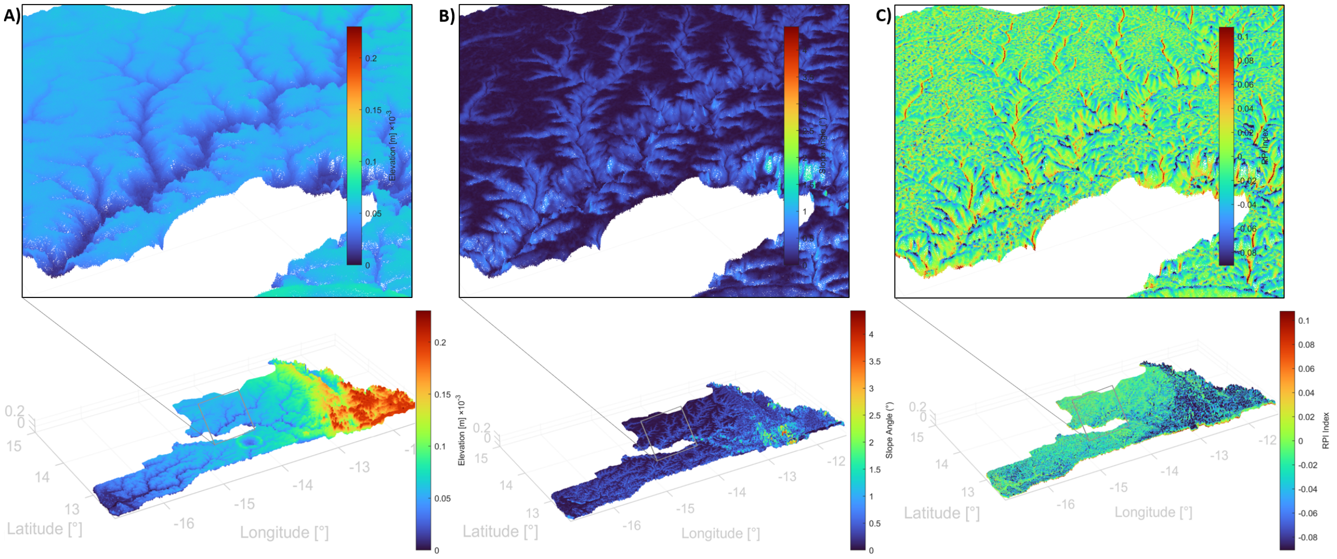

Figure 3. Regional terrain analysis for Casamance and Senegal Oriental. (A) Digital elevation model; (B) Slope angle distribution; (C) Runoff Potential Index (RPI) for upland-lowland differentiation. Blue areas indicate runoff-prone upland zones (negative RPI), while red areas represent water-retaining lowland zones (positive RPI).

additional reference demonstration. Panel A shows digital elevation models for each area, Panel B presents slope angle distributions, and Panel C displays the computed Runoff Potential Index (RPI) that integrates local curvature (via Laplacian) and slope steepness to characterize terrain-driven water divergence patterns across diverse topographic settings.

Negative RPI values correspond to convex upland forms (e.g., ridgelines and steep slopes) that promote rapid surface runoff and minimal water retention. In contrast, positive RPI values are associated with concave lowland areas where water tends to accumulate or infiltrate, increasing drought resilience. The spatial distributions in Figure 2C demonstrate how RPI values vary across different regional terrain characteristics, maintaining consistent physical interpretation across diverse topographic settings.

Scaling this approach to regional analysis, Figure 3 presents the complete terrain characterization across Ziguinchor, Sédhiou, Kolda, Tambacounda, and Kédougou regions at approximately 51-meter spatial resolution. The regional-scale application reveals distinct hydrological zones across the landscape, with upland areas (blue) exhibiting high water divergence and runoff potential at both major elevation peaks and subtle microtopographic variations, while lowland zones (red) demonstrate water convergence and retention capacity in valley systems and floodplains. This regional mapping enables identification of drought-vulnerable versus resilient agricultural areas based on inherent terrain characteristics.

Drought stress patterns and adaptation strategies through CERES-Rice modeling and Earth observation integration

Earth observation systems provide spatially-complete environmental datasets essential for drought stress analysis across agricultural regions lacking comprehensive ground monitoring networks. Satellite-derived Digital Elevation Models (51-meter resolution) enable precise Runoff Potential Index calculations, while SoilGrids generates standardized soil texture data at 250-meter resolution for hydraulic conductivity modeling. NASA POWER satellite-based precipitation observations at 0.5° resolution provide temporally consistent meteorological forcing specifically validated for DSSAT crop modeling protocols[46–48]. This integrated Earth observation framework ensures complete spatial coverage across Senegal's territory, enabling CERES-Rice simulations to quantify drought stress patterns and optimize sowing strategies with unprecedented accuracy impossible through conventional ground-based data networks.

Soil texture characterization from satellite-derived observations

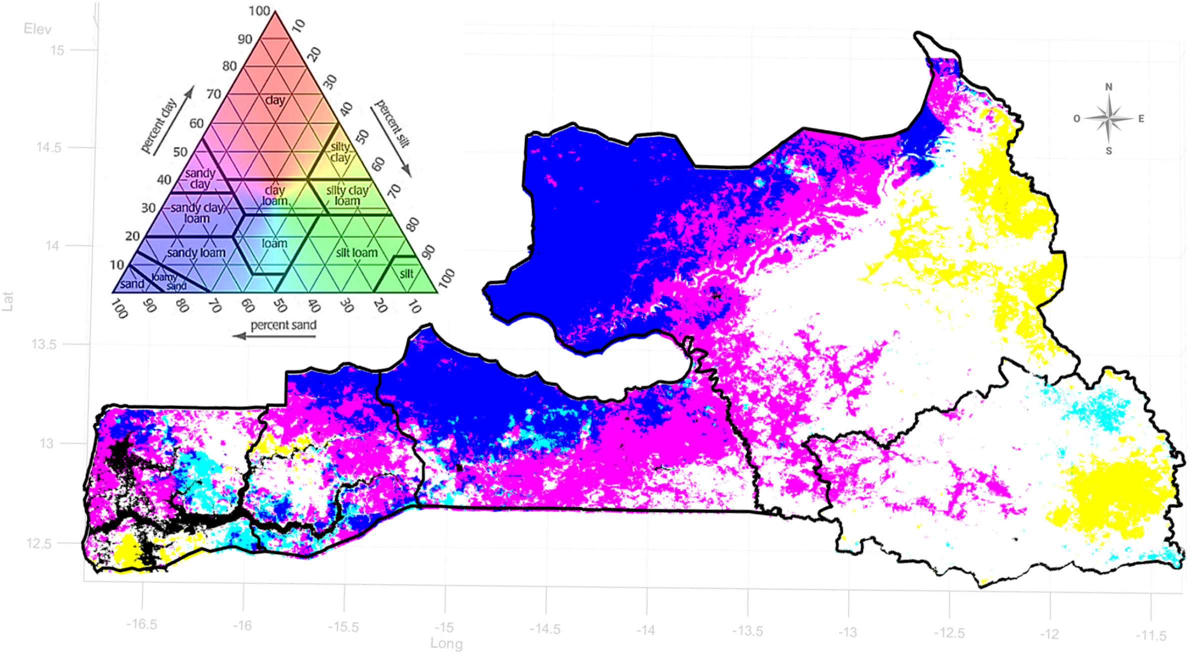

Figure 4. Soil texture composition and distribution at 15 cm depth, based on satellite-derived Earth observation. The RGB color space is used to represent the relative proportions of sand, silt, and clay across the study area, providing an intuitive and information-rich visualization of soil texture. White corresponds to clay loam, located near the center of the texture triangle and known for its balanced water retention and drainage properties. The most prevalent soil types include sandy loam (blue), sandy clay (purple), and clay loam (white), while loam (cyan) and silty clay (yellow) appear less frequently. This classification supports drought vulnerability assessment by identifying spatial patterns in soil hydraulic behavior.

Following the terrain-based runoff analysis, soil texture characterization provides the complementary subsurface perspective essential for comprehensive drought vulnerability assessment. Soil texture, a key determinant of water retention and infiltration capacity, plays a fundamental role in mediating the landscape's response to drought. Based on SoilGrids satellite-derived Earth observation datasets, the spatial distribution of soil texture at a depth of 15 cm reveals a heterogeneous mosaic of sand, silt, and clay compositions. These components are visualized in Figure 4 using an innovative RGB color space mapping within the soil texture triangle. This approach intuitively encodes complex textural information into a perceptually accessible format. In this representation, white denotes clay loam soils located near the triangle's center, a texture class of particular relevance due to its balanced hydraulic properties.

Soil texture directly governs hydraulic conductivity, the rate at which water infiltrates through the soil, and is a key determinant of how landscapes respond to rainfall and drought. Using satellite-derived soil texture maps, we spatially estimated infiltration capacity across the region. The dominant soil types include sandy loam (blue), sandy clay (purple), and clay loam (white), with estimated saturated hydraulic conductivities of approximately 30 mm/h, 5 mm/h, and 2.5 mm/h, respectively. Less common textures such as loam (cyan, 10 mm/h) and silty clay (yellow, 0.5 mm/h) are also present and may influence localized water retention. These estimates enable a physically grounded integration of subsurface dynamics into drought vulnerability analysis, complementing terrain-based runoff assessment with infiltration capacity.

Rainfall Distribution

Precipitation patterns derived from NASA POWER satellite-based observations reveal distinct seasonal and interannual variability that directly influences agricultural water stress dynamics. Figure 5 presents a comprehensive analysis of rainfall distribution from 2000 to 2020, demonstrating the temporal structure of precipitation across the study region. The left panel displays monthly rainfall magnitudes over the 20-year period, revealing pronounced seasonal patterns consistent with the characteristic climate of the Casamance region, where the rainy season generally lasts from June to October, followed by a dry season from November to May[49].

The probabilistic analysis in the right panel quantifies rainfall distribution characteristics through empirical density estimation fitted with a Gaussian curve. Peak rainfall occurs during August-September, while the dry season (November-April) exhibits minimal precipitation. This statistical characterization reveals distinct seasonal patterns with pronounced wet season concentration and extended dry periods. The temporal variability directly informs CERES-Rice water balance calculations, where the 20-year precipitation record (2000-2020) demonstrates high seasonal concentration of rainfall essential for rainfed rice production. Understanding these precipitation dynamics is crucial for determining optimal planting dates, as rainfall timing and magnitude determine soil water availability during sensitive phenological stages, particularly flowering and grain filling periods when drought stress most significantly impacts yield potential[50–52].

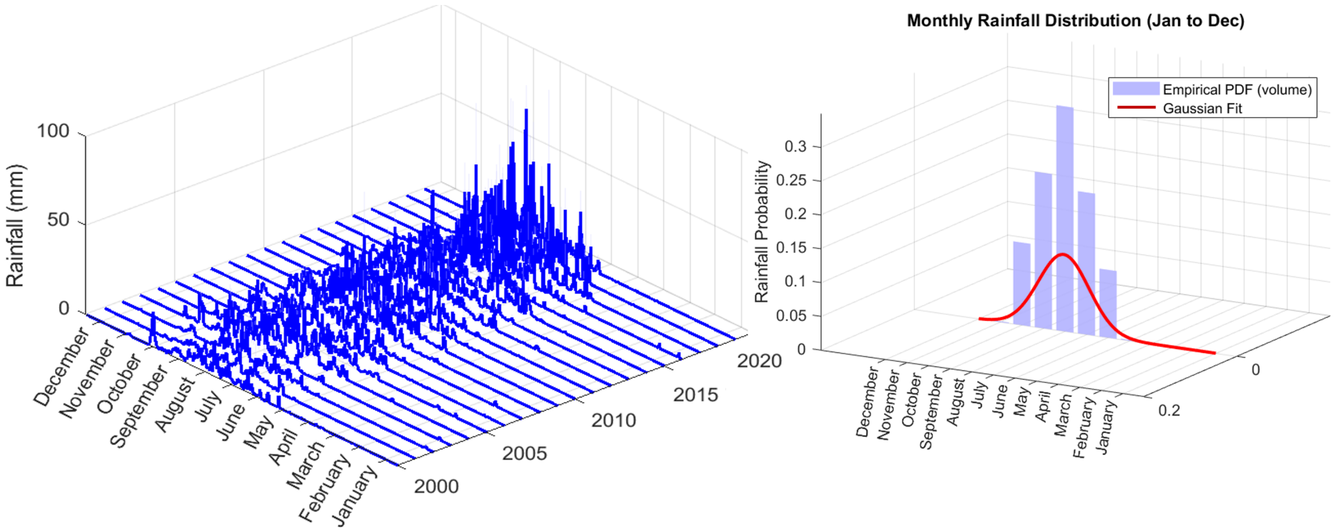

Figure 5. Rainfall seasonality and interannual variability (2000–2020). The left panel illustrates monthly rainfall magnitudes over a 20-year period, revealing strong seasonal patterns. The right panel presents the probabilistic distribution of rainfall across months, with a Gaussian curve fitted to the empirical density. Together, these visualizations characterize the temporal structure and predictability of precipitation, informing drought risk modeling.

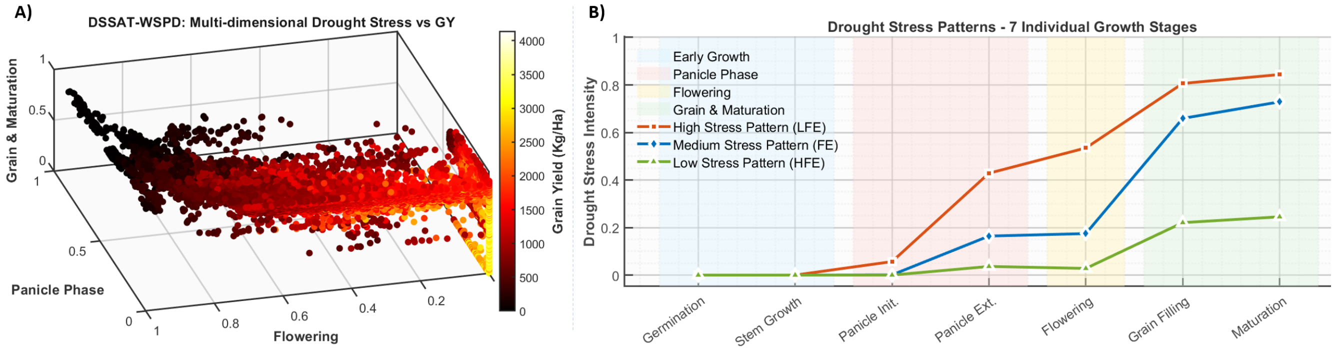

Figure 6. Drought stress characterization and phenological response patterns in rice: (A) Three-dimensional scatter plot showing the relationship between drought stress intensity across three phenological phases (Panicle Phase, Flowering, and Grain & Maturation) and resulting grain yield from 20-year DSSAT-WSPD simulations, with color gradient representing yield magnitude (kg/ha), and (B) Drought stress progression patterns across seven individual growth stages for three stress patterns classifications, with background shading indicating phenological phase groupings (Early Growth: blue, Panicle Phase: red, Flowering: yellow, Grain & Maturation: green).

CERES-Rice driven drought stress patterns recognition

Multi-dimensional analysis of drought stress patterns revealed complex relationships between phenological timing, stress intensity, and grain yield outcomes (Figure 6). The three-dimensional visualization demonstrated that yield reductions were most pronounced when high stress levels occurred simultaneously across multiple phenological periods, particularly during reproductive phases. Yields exceeding 3,000 kg/ha were predominantly associated with favorable environmental conditions across all phases, while severe yield reductions below 1,000 kg/ha occurred when stress intensities exceeded 0.5 units during critical reproductive periods.

Phenological stress progression patterns revealed distinct temporal patterns for each environmental favorability classification (Figure 6B). Low Favorable Environments (LFE) exhibited characteristic stress escalation, starting near zero during germination

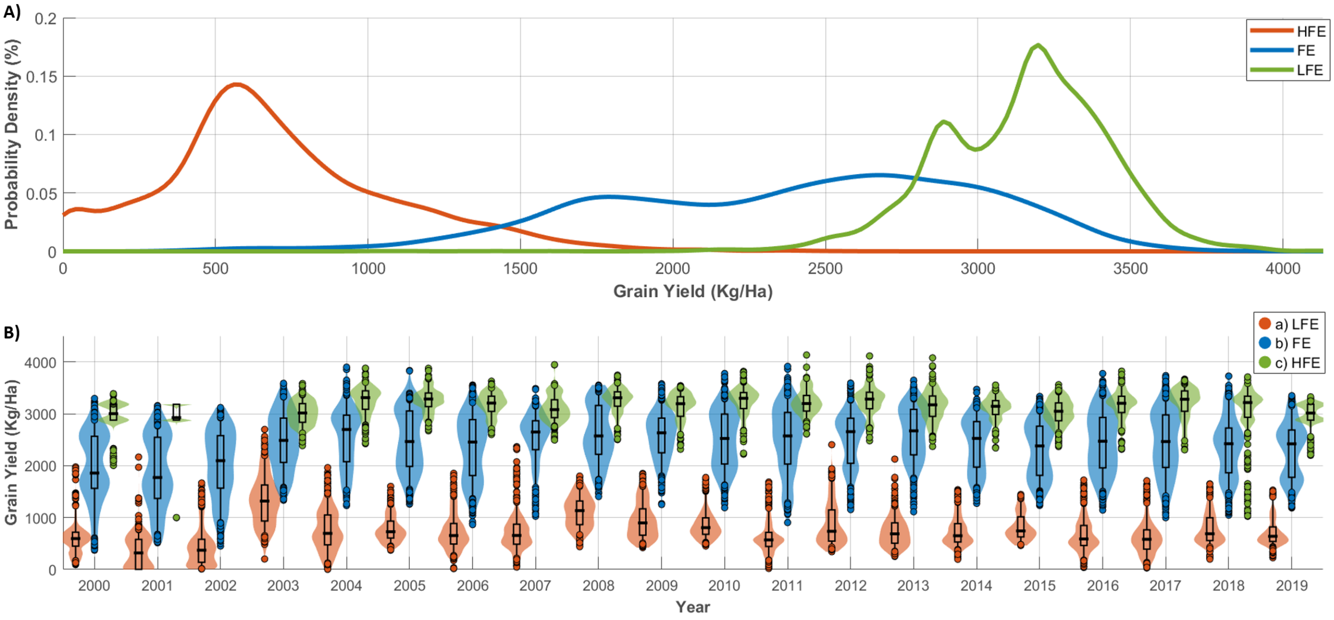

Figure 7. Characterization of rice yield distributions under variable drought stress regimes. Panel (a) presents kernel density estimation curves illustrating the probability density functions of grain yield for three drought frequency classes derived from cluster analysis of 20-year DSSAT-WSPD simulations. Panel (b) shows annual violin plots (2000-2019) depicting yield distribution patterns by drought stress classification: Low Frequency Events (LFE), Frequent Events (FE), and High Frequency Events (HFE). Violin plots combine probability density shapes with embedded quartile box plots and outlier identification.

and stem growth, then showing rapid increases from 0.05 to 0.43 during panicle initiation and extension phases, followed by sustained high stress intensities reaching 0.52 at flowering and culminating at 0.83 during grain filling and maturation. Favorable Environments (FE) showed moderate stress levels with gradual progression from near zero in early stages to 0.17 during panicle phases, reaching maximum intensity of 0.18 during flowering, then maintaining stable levels around 0.65-0.72 through grain filling and maturation. High Favorable Environments (HFE) maintained consistently low stress throughout all growth stages, with values remaining below 0.05 during vegetative phases and only reaching 0.21-0.23 during the final grain filling and maturation stages, representing optimal growing conditions with minimal drought impact.

The analysis of rice grain yield variability under different drought stress regimes, based on 20 years of DSSAT-WSPD simulation data (2000–2019), revealed three statistically distinct yield response distributions (Figure 7). Kernel Density Estimation (KDE) analysis employing Gaussian kernels with Silverman's bandwidth optimization identified complex multimodal yield distributions that deviated significantly from normal distribution assumptions across environmental favorability categories.

Low Favorable Environments (LFE) demonstrated a highly concentrated unimodal distribution centered at 600 kg/ha, representing consistently low yields under high drought stress conditions. Favorable Environments (FE) displayed a broad, relatively uniform distribution spanning 1,500–3,000 kg/ha, reflecting intermediate environmental conditions with variable yield performance. In contrast, High Favorable Environments (HFE) exhibited a distinctive bimodal distribution with peaks at approximately 3,000 kg/ha and 3,400 kg/ha, indicating two predominant high-yield scenarios under optimal growing conditions.

Temporal stability analysis using violin plots quantified the persistence of these distributional characteristics using coefficient of variation (CV = $(\sigma/\mu) \times 100$) across the 20-year simulation period (Figure 7b). LFE maintained significantly lower median yields (798 ± 45 kg/ha, CV = 52%) with high inter-annual variability, while FE exhibited intermediate performance ($2,284 \pm 156$ kg/ha, CV = 31%) and HFE sustained stable high productivity ($3,187 \pm 89$ kg/ha, CV = 18%). The temporal consistency of these distribution patterns validates the predictive reliability of the environmental favorability classification framework for rice yield forecasting under variable climatic scenarios.

Building upon the phenological stress patterns and yield distribution analysis, the spatial-temporal examination of the Target Population of Environments (TPE) for drought stress reveals the geographic manifestation of these environmental favorability classifications across Senegal's agricultural landscape (Figure 8). The spatial analysis demonstrates that the HFE, FE, and LFE classifications identified through temporal yield analysis exhibit distinct geographic distributions that vary systematically across the five sequential sowing dates (S1-S5). Environment favorability mapping shows a clear temporal progression, with early sowing dates (S1-S2) characterized by predominantly High Favorable Environment (HFE) conditions in the western and southern regions, consistent with the optimal growing conditions that sustained stable high productivity (3,187 ± 89 kg/ha, CV = 18%) observed in the temporal analysis. As the sowing season advances (S3-S5), there is a notable shift toward Favorable Environment (FE) and Least Favorable Environment (LFE) conditions, particularly in the northern and eastern areas, reflecting the transition toward the intermediate performance (2,284 ± 156 kg/ha, CV = 31%) and low-yield scenarios (798 ± 45 kg/ha, CV = 52%) respectively. The coefficient of variation analysis demonstrates varying levels of temporal stability across the agricultural landscape, with High Stability (HS) zones consistently observed in the western coastal regions across all sowing dates, indicating reliable environmental conditions that align with the low inter-annual variability (CV = 18%) characteristic of HFE conditions. Conversely, the central and northern regions exhibit Middle Stability (MS) to Low Stability (LS) patterns, suggesting higher inter-annual variability consistent with the elevated coefficients of variation observed in FE

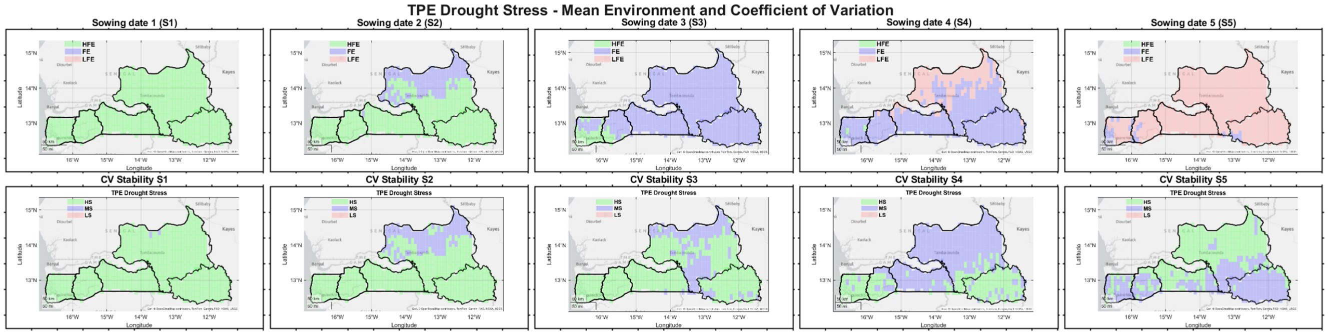

Figure 8. Target Population of Environments (TPE) drought stress characterization for agricultural planning in Senegal across five sequential sowing dates (S1-S5). Upper panels display mean environment favorability patterns: High Favorable Environment (HFE, green), Favorable Environment (FE, blue), and Least Favorable Environment (LFE, orange). Lower panels show coefficient of variation analysis indicating temporal stability: High Stability (HS, green), Middle Stability (MS, blue), and Low Stability (LS, orange).

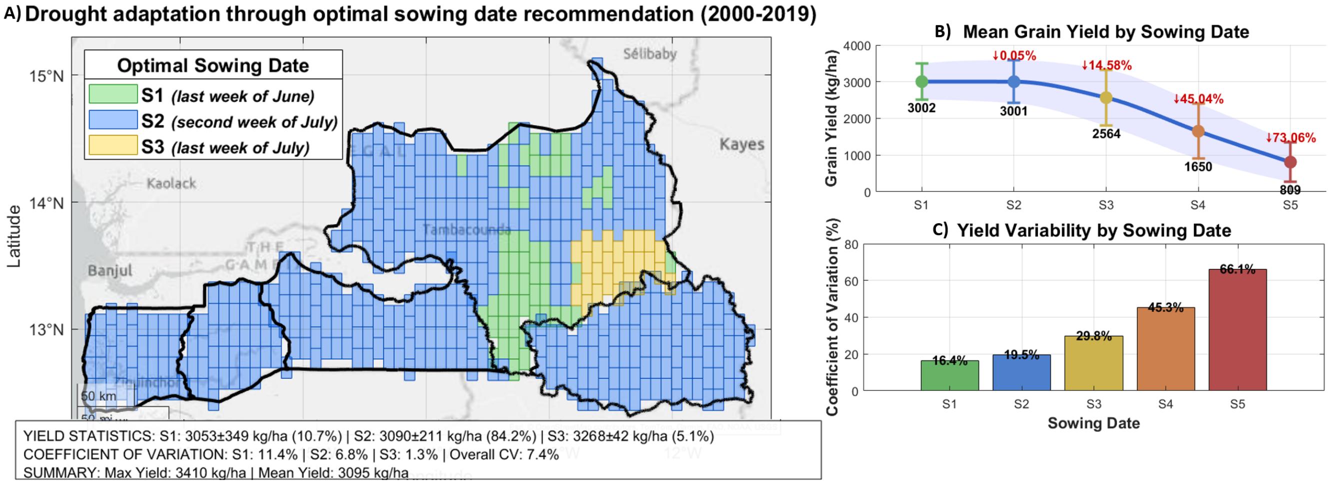

Figure 9. Drought adaptation through optimal sowing date recommendations in Senegal (2000–2019). (A) Spatial distribution of optimal sowing dates: S1 (last week of June, green), S2 (second week of July, blue), and S3 (last week of July, yellow). S2 is optimal for the majority of the territory (84.2%), achieving yields of 3090±211 kg/ha with low variability (CV=6.8%). S3 shows the highest yields (3268±42 kg/ha) but is optimal only in a specific region of Casamance (5.1% of locations). (B) Mean grain yield demonstrates a clear decline with delayed sowing, with S1 and S2 maintaining similar performance (3000 kg/ha) before sharp reductions in later dates. Percentage changes indicate yield losses of 14.6%, 45.0%, and 73.1% for S3, S4, and S5 respectively, compared to S1. (C) Yield variability analysis reveals increasing coefficient of variation with delayed sowing (16.4% to 66.1%), highlighting the trade-off between yield potential and risk. Early sowing dates (S1–S2) provide stable yields with manageable variability, while late sowing (S4–S5) introduces substantial production risk despite potential high yields in favorable conditions.

and LFE environments. The transition from S1 to S5 shows a progressive deterioration in both favorability and stability, with S4 and S5 displaying the most heterogeneous spatial distribution of environmental conditions, indicating that optimal sowing windows occur during the early season (S1-S2) when spatial patterns align with the temporal characteristics of high-yield, low-variability environments identified in the phenological analysis.

Drought adaptation strategies through optimal sowing date recommendations

Building upon the Target Population of Environments analysis, the spatial analysis of optimal sowing dates across Senegal (2000–2019) identified three distinct sowing windows with varying geographic distributions (Figure 9A). S2 (second week of July) represented the optimal choice for 84.2% of the territory, achieving yields of 3090±211 kg/ha. S1 (last week of June) was optimal for 10.7% of locations with yields of 3053±349 kg/ha, while S3 (last week of July) was optimal for only 5.1% of locations, concentrated primarily in the Casamance region, yielding 3268±42 kg/ha.

Mean grain yield analysis across five sowing dates revealed a progressive decline pattern (Figure 9B). S1 and S2 maintained similar performance levels at 3002 and 3001 kg/ha respectively. Subsequent sowing dates showed progressive yield reductions: S3 declined 14.6% to 2564 kg/ha, S4 dropped 45.0% to 1650 kg/ha, and S5 experienced a 73.1% reduction to 809 kg/ha compared to S1.

Yield variability analysis demonstrated increasing temporal instability with delayed sowing (Figure 9C). The coefficient of variation increased systematically from 16.4% for S1 to 66.1% for S5. S2 exhibited moderate variability at 19.5%, while S3 showed 29.8% variability despite achieving the highest absolute yields in its optimal zones.

The geographic concentration of S3 optimality in Casamance corresponded to areas with extended rainfall patterns exceeding 1000 mm annually. The remaining territory showed preference for earlier sowing dates, with S2 demonstrating the broadest spatial applicability while maintaining yield stability. S4 and S5 showed increasingly restricted optimal zones with elevated production risk across all geographic regions.

Comparison between terrain-based runoff potential and sowing date optimization

Building upon the drought stress characterization and Target Population of Environments analysis, the integration of terrain-based water redistribution patterns with optimal sowing strategies provides additional insights into site-specific drought adaptation mechanisms. The Runoff Potential Index (RPI) analysis, derived from high-resolution satellite Digital Elevation Model data at 51-meter spatial resolution, was spatially aggregated at the 506 DSSAT simulation locations using a 2.5-km search radius to characterize terrain-driven water redistribution patterns across Senegal's agricultural landscape.

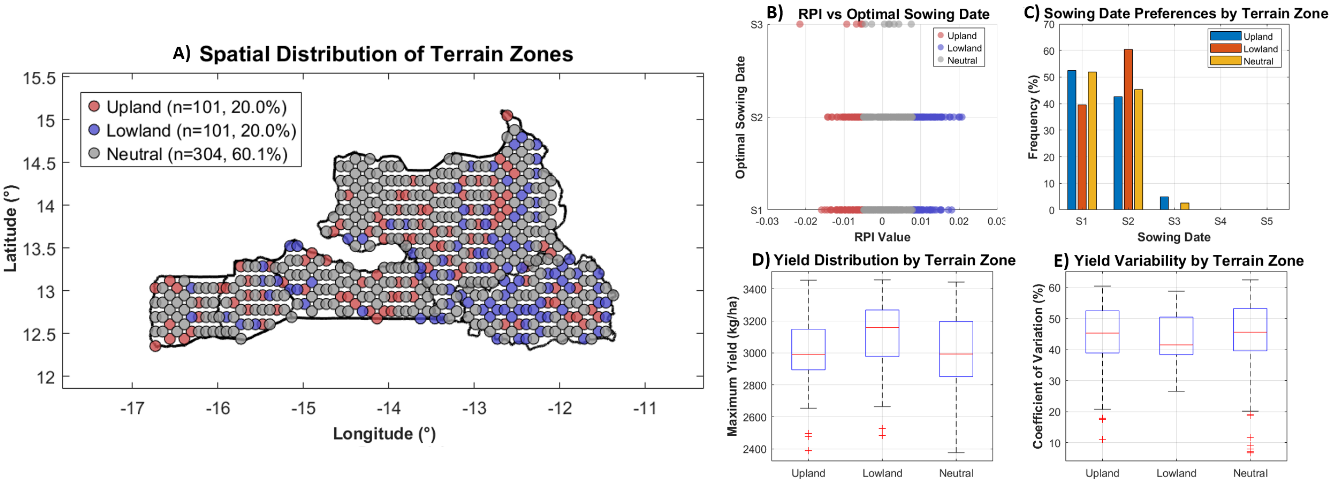

Figure 10. Integration of terrain-based runoff potential with sowing date optimization in Senegal (2000–2019). (A) Spatial distribution of terrain zones based on Runoff Potential Index (RPI): Upland areas (red, 20.0%) represent runoff-prone terrain with negative RPI values, Lowland areas (blue, 20.0%) indicate water-retaining terrain with positive RPI values, and Neutral zones (gray, 60.1%) represent intermediate conditions. (B) Relationship between RPI values and optimal sowing dates shows terrain-dependent preferences, with most optimal dates concentrated in S1–S2 across all terrain types. (C) Sowing date preferences reveal that all terrain zones favor early sowing (S1–S2), with S2 being the most frequent optimal choice (40–60% across zones), while later sowing dates (S4–S5) are rarely optimal. (D) Yield distributions demonstrate that Lowland areas achieve slightly higher median yields (3200 kg/ha) compared to Upland (3000 kg/ha) and Neutral areas (3100 kg/ha). (E) Yield variability analysis shows similar coefficient of variation patterns across terrain zones (40–55%), indicating that terrain-based water redistribution provides consistent drought buffering effects regardless of topographic position.

Terrain classification employed percentile-based thresholds (20th and 80th percentiles) applied to RPI values, resulting in three distinct hydrological zones: Upland areas (20.0%, n=101) characterized by negative RPI values (-0.022 to -0.005) indicating runoff-prone terrain; Lowland areas (20.0%, n=101) with positive RPI values (0.008 to 0.021) representing water-retaining depressions; and Neutral zones (60.1%, n=304) with intermediate RPI values (-0.005 to 0.008) indicating balanced water redistribution patterns (Figure 10A). The spatial distribution revealed scale-dependent patterns, with Lowland areas predominantly concentrated in the eastern montane regions where high-resolution DEM analysis captures numerous water-retaining microtopographic depressions, while Upland areas were more prevalent in the western coastal plains characterized by uniform terrain and lateral water flow.

The relationship between terrain-based water redistribution and optimal sowing dates demonstrated limited influence of topographic position on temporal agricultural strategies (Figure 10B). All terrain zones exhibited consistent preference for early sowing windows, with S2 (second week of July) representing the optimal choice across 40–60% of locations regardless of RPI classification. This uniformity in sowing date preferences across terrain types indicates that seasonal precipitation timing determines optimal sowing strategies, while local terrain advantages do not significantly alter these recommendations, consistent with the TPE analysis showing early sowing dates (S1–S2) aligned with High Favorable Environment conditions across diverse geographic contexts.

Yield performance analysis revealed terrain-mediated yield differences of approximately 6–10% between zones (Figure 10D). Lowland areas achieved yields 200 kg/ha higher (3200 kg/ha) compared to Upland areas (3000 kg/ha) and 100 kg/ha higher than Neutral zones (3100 kg/ha). However, yield variability patterns remained consistent across terrain classifications (Figure 10E), with coefficient of variation for yields at optimal sowing dates ranging from 40–55% across all terrain zones, indicating comparable inter-annual stability independent of topographic position. These terrain-based yield differences (200–300 kg/ha) are substantially smaller than the variability associated with sowing date optimization, where delayed planting from S1–S2 to S4–S5 resulted in yield reductions exceeding 1500 kg/ha, reinforcing the primacy of temporal over spatial optimization strategies.

The integration of RPI analysis with the previously established environmental favorability classifications (HFE, FE, LFE) demonstrates that terrain-based water redistribution operates as a secondary modifying factor within the broader framework of climate-driven agricultural constraints. While Lowland areas provide systematic yield advantages and enhanced water stress mitigation through improved water retention, these benefits are insufficient to justify alternative sowing strategies that deviate from the climatically-optimal S1–S2 timing window. This finding supports the spatial pattern observed in the TPE analysis, where western coastal regions maintained High Stability conditions across multiple sowing dates, suggesting that areas with favorable terrain characteristics (water retention) combined with optimal climatic timing (early sowing) represent the most resilient agricultural zones for drought adaptation strategies.

Discussion

Analytical superiority of RPI over conventional topographic indices

The comparative analysis between the Runoff Potential Index (RPI) and the widely used Topographic Wetness Index (TWI) reveals fundamental differences in their capacity to represent terrain-driven hydrological processes. RPI consistently outperforms TWI in both morphological sensitivity and numerical stability, particularly in low-gradient and transition zones where traditional slope-dependent indices often fail.

Across all synthetic terrain scenarios, ranging from deep concavities and convex hilltops to subtle undulations and flat reference surfaces, RPI provides physically interpretable and hydrologically meaningful values. For instance, RPI identifies water-retentive zones with positive values and runoff-prone uplands with negative values, maintaining a dynamic and continuous response to terrain curvature and slope. In contrast, TWI yields nearly identical values across morphologically distinct locations, such as crater boundaries and hill slopes, failing to detect functional hydrological differences. This limitation is especially critical in the analysis of subtle morphological transitions, where RPI captures the directional nature of water flow changes (e.g., -0.013 vs +0.013 at opposite curvature points), while TWI produces nearly indistinguishable outputs (e.g., 23.126 vs 23.254).

A particularly stark contrast emerges in flat or near-flat regions, where TWI exhibits extreme instability. In the reference flat point of the synthetic field, TWI reaches a value of 48.660, higher than in any concave or convex zone, despite the lack of hydrological gradient. This behavior undermines its reliability for automated analysis across large-scale datasets. RPI, on the other hand, remains stable and neutral (value = 0.000) under these conditions, demonstrating its mathematical robustness and conceptual soundness.

Moreover, the successful application of RPI across multiple spatial resolutions, from 2.5 m synthetic surfaces to 51 m satellite-derived regional maps, demonstrates its scalability and adaptability to remote sensing workflows. Unlike TWI, which depends heavily on slope calculations prone to amplification errors in low-gradient terrain, RPI integrates curvature (via Laplacian) and slope in a way that preserves the topographic signal and avoids the instability. This quality enables its deployment across UAV imagery, local DEMs, and regional elevation datasets, providing consistent classification of upland (runoff-prone) and lowland (water-retentive) areas across diverse landscapes.

Finally, RPI's ability to detect centimeter-scale elevation differences (e.g., 0.7–1.8 m across microtopographic waves and craters) further enhances its utility for precision agriculture, particularly in drought-prone environments where small-scale terrain variation can substantially affect water retention and crop stress. The morphological transition zones, where RPI detects meaningful directional hydrological shifts and TWI does not, illustrate a conceptual boundary: traditional indices are unable to capture the directional logic of terrain-induced water dynamics. In contrast, RPI encodes this information inherently through its mathematical formulation.

RPI demonstrates clear analytical superiority over conventional indices like TWI by combining physical interpretability, numerical stability, and morphological sensitivity. These findings collectively establish RPI as a technically superior and scalable solution for terrain-based hydrological modeling, particularly in flat or heterogeneous landscapes where traditional indices often misrepresent or oversimplify critical water redistribution processes.

Integration of earth observation–derived environmental data for mechanistic crop modeling

The results confirm the viability of a fully Earth Observation–based data architecture to support mechanistic crop modeling in data-scarce regions. This framework integrates both direct remote sensing inputs, such as satellite-derived Digital Elevation Models (51 m resolution) used to compute the Runoff Potential Index (RPI), and derived Earth Observation products, including SoilGrids soil texture maps (250 m resolution) and NASA POWER meteorological datasets generated from satellite observations and physical modeling (0.5° resolution). While DEMs represent direct measurements from satellite sensors, SoilGrids and NASA POWER synthesize multiple data sources, including remote sensing, field observations, and numerical modeling, to provide globally consistent, spatially continuous environmental variables, as recommended by the DSSAT modeling framework in its protocols for large-scale applications.

Together, these datasets form a physically coherent and spatially harmonized environmental baseline for drought stress simulation. Topographic information from DEMs captures terrain-driven water redistribution via RPI, while SoilGrids provides subsurface hydraulic characteristics, such as saturated conductivity estimates ranging from $\sim$30 mm/h (sandy loam) to $\sim$2.5 mm/h (clay loam). NASA POWER complements these inputs by supplying meteorological forcing variables validated for process-based crop modeling in tropical and subtropical climates. This dual integration, combining terrain morphology from remote sensing with subsurface and climatic information from Earth Observation, enables high-resolution, site-specific drought vulnerability assessment and adaptive agricultural planning, even in the absence of in-situ environmental monitoring.

Phenology-specific drought stress modeling and the limitations of water balance approaches

The CERES-Rice model, as implemented in DSSAT simulations and driven entirely by Earth Observation–derived inputs, revealed distinct temporal patterns of drought stress progression across varying environmental favorability classes. Highly Favorable Environments (HFE) maintained minimal stress levels throughout the season, with values below 0.05 during vegetative stages and peaking only modestly (0.21–0.23) during grain filling. Favorable Environments (FE) exhibited a more gradual stress accumulation pattern, with intensities rising from near zero in early growth to a maximum of 0.18 at flowering. In contrast, Least Favorable Environments (LFE) demonstrated severe and rapid stress escalation, with intensities increasing from 0.05 to over 0.8, particularly during panicle initiation and reproductive phases, periods known to be highly sensitive to water deficit.

These patterns, derived from 20-year DSSAT simulations, translated into statistically distinct grain yield distributions: LFE conditions resulted in a narrow unimodal distribution centered around 600 kg/ha (CV = 52%), FE exhibited a broader, uniform distribution between 1,500 and 3,000 kg/ha (CV = 31%), while HFE showed a bimodal high-yield pattern (3,000–3,400 kg/ha, CV = 18%). The mechanistic modeling approach captures the temporal alignment between environmental favorability and crop phenology, but it also reveals structural limitations in conventional water balance models such as those implemented in DSSAT. In particular, DSSAT employs a simplified "bucket" model of soil water dynamics, which assumes vertical redistribution only and neglects lateral water flow. As a result, terrain-induced hydrological differences, such as enhanced water retention in concave lowland areas and increased runoff in convex upland zones, as identified by the Runoff Potential Index (RPI), are not adequately reflected in crop stress outcomes.

Despite clear differences in topographic water accumulation potential, all RPI terrain classes (upland, neutral, lowland) showed nearly identical preferences for early sowing dates (S1–S2), and exhibited comparable yield variability patterns (CV = 40–55%), suggesting that DSSAT does not sufficiently account for topographic water redistribution processes. This reveals a conceptual limitation in current mechanistic models: while temporally dynamic and phenologically sensitive, they remain spatially constrained by the assumption of homogeneous vertical water movement. Integrating terrain-aware hydrological models into crop simulation frameworks could therefore improve their ability to represent local drought buffering capacity and optimize site-specific agricultural strategies in heterogeneous landscapes.

Critical comparison between terrain-based and mechanistic models: Structural constraints of the bucket approach

The comparative analysis between the terrain-based Runoff Potential Index (RPI) and the mechanistic CERES-Rice model implemented in DSSAT reveals fundamental divergences in how water redistribution is conceptualized, represented, and integrated into crop stress modeling. RPI captures spatial heterogeneity in hydrological behavior using only topographic data, identifying both water-retentive lowland zones and runoff-prone upland areas with a high degree of spatial resolution. In contrast, DSSAT operates under a vertically constrained water balance approach, commonly described as a "bucket" model, which assumes homogeneous vertical redistribution of soil water and omits lateral flow processes. This structural limitation leads to notable inconsistencies in drought stress outcomes: although RPI clearly distinguishes terrain positions with contrasting water retention potential, DSSAT simulations exhibit nearly uniform sowing date preferences and similar yield variability across all terrain classes. Specifically, lowland areas identified by positive RPI values, expected to provide hydrological buffering during dry periods, do not show reduced stress or enhanced yield stability in the simulations, suggesting that topographic effects are functionally invisible to the model. Similarly, upland areas with high runoff potential do not exhibit increased vulnerability in the modeled outputs. This disconnect underscores the inability of current bucket-based mechanistic models to internalize terrain-induced hydrological gradients, even when such gradients are physically evident and spatially coherent. While DSSAT excels in modeling phenological timing and vertical water dynamics, its lack of lateral hydrology introduces a conceptual blind spot, particularly in heterogeneous landscapes. The integration of RPI into the analytical workflow thus exposes the need for hybrid modeling approaches that bridge the gap between topographic realism and process-based simulation. Incorporating terrain-aware hydrological components into crop models could enable more accurate site-specific adaptation strategies, especially in drought-prone regions where microtopographic effects critically influence water availability.

Conclusions

This study demonstrates that integrating terrain-based hydrological indices derived from remote sensing with mechanistic crop models significantly enhances our understanding of drought vulnerability in rainfed agricultural systems. The Runoff Potential Index (RPI), developed from satellite-based Digital Elevation Models, offers a physically interpretable, numerically stable, and scalable alternative to conventional slope-dependent indices such as the Topographic Wetness Index (TWI). RPI successfully distinguishes runoff-prone uplands from water-retentive lowlands, capturing microtopographic gradients that are critical for site-specific water availability. Its consistent behavior across spatial resolutions, from synthetic terrains to regional applications, positions it as a robust terrain diagnostic for hydrological analysis.

The integration of RPI with Earth Observation-derived environmental datasets, including soil texture (SoilGrids) and climate data (NASA POWER), enables fully remote and spatially continuous inputs for process-based modeling using DSSAT. However, the comparative analysis reveals a conceptual mismatch: while RPI captures lateral water redistribution driven by terrain morphology, DSSAT operates under a vertically constrained "bucket" model that fails to incorporate such topographic effects. As a result, the hydrological advantages identified through terrain analysis are not adequately reflected in crop stress predictions, underscoring the need for hybrid modeling frameworks that bridge this gap.

Study Limitations and Future Directions

While this study advances the integration of terrain analysis with crop modeling, several methodological limitations should be acknowledged in the interpretation of results.

First, the CERES-Rice model employs a simplified “bucket” approach for soil water dynamics, assuming predominantly vertical water redistribution and neglecting lateral flow processes. This limitation becomes particularly relevant when contrasted with the RPI analysis, which explicitly captures terrain-driven lateral water redistribution patterns that may influence local drought resilience but are not adequately represented in the crop model’s hydrological framework.

Second, spatial resolution constraints may limit the detection of critical microtopographic variations. The SRTM DEM data (30-meter resolution) may not capture centimeter-scale elevation differences that significantly influence water retention at field scales, while NASA POWER meteorological data (50 km resolution) represent spatial averages that may smooth important local climatic variability affecting drought stress patterns.

Third, the study relies on mechanistic modeling approaches due to the inherent limitations of field-based validation in the study region, where comprehensive yield monitoring networks are absent due to logistical complexity, high costs, and limited infrastructure in remote agricultural areas. While this constraint necessitates the use of satellite-driven crop modeling frameworks, it limits direct empirical validation of simulated drought stress responses against observed field performance.

Fourth, the spatial aggregation methodology employed for RPI analysis, utilizing a 2.5-km search radius around simulation points, may attenuate fine-scale topographic heterogeneity that influences localized water retention patterns. This smoothing effect could potentially affect the representation of terrain-based drought buffering capacity in highly heterogeneous landscapes.

Despite these limitations, the integration of satellite-derived environmental data with mechanistic crop modeling provides a scalable and systematic approach for drought vulnerability assessment in data-scarce regions, while the identified constraints highlight opportunities for future methodological refinements incorporating more sophisticated hydrological representations and higher-resolution environmental datasets.

Future work will build upon the development of the *Runoff Potential Index Simulation Toolbox* (Version 1.0.0), a MATLAB-based application that implements a 3D physics-based simulation of terrain-mediated water flow. This toolbox provides real-time visualization of surface water dynamics and automated RPI computation, specifically designed for low-gradient agricultural landscapes. It offers a practical platform for integrating curvature-based hydrological insights into operational drought risk assessment, precision agriculture, and scientific training on terrain-mediated water redistribution. Future research will focus on coupling this toolbox with mechanistic crop models to enable terrain-informed simulations, improving sowing date recommendations and field-scale water management. Additional efforts will include UAV-based assessment of RPI outputs and scaling the framework for continental applications across drought-prone regions. Overall, this research lays the foundation for topography-aware, remote sensing-driven decision support systems for climate-resilient agricultural planning.

Methods

Study Area and Spatial Coverage

The study was conducted in southern and southeastern Senegal, encompassing the Casamance and Eastern Senegal regions. These areas, specifically Ziguinchor, Sédhiou, Kolda, Tambacounda, and Kédougou, are characterized by diverse agroecological conditions and a predominantly rainfed rice-based agricultural system. The climate is tropical with distinct wet and dry seasons, driven by the West African Monsoon. Annual rainfall typically ranges from 800 to 1,500 mm, concentrated between June and October, making crop production highly sensitive to seasonal precipitation dynamics.

The Casamance region spans approximately 28,350 km², while the Eastern Senegal region covers around 42,364 km², totaling over 70,000 km². The terrain in these areas exhibits low to moderate relief, with microtopographic variations on the order of 20 to 80 cm that critically influence surface runoff and water retention dynamics. A total of 506 georeferenced locations were selected to provide spatial coverage for environmental characterization and crop model simulations, representing a sampling resolution of approximately one point per 140 km². These locations span diverse topographic and edaphoclimatic conditions, enabling a representative assessment of terrain-induced drought vulnerability. All geospatial analyses were performed using data projected to the WGS 84 / UTM Zone 28N coordinate system and clipped to Senegal's national boundaries.

Data Sources and Preprocessing

Topographic Data

Topographic information was derived from the Shuttle Radar Topography Mission (SRTM) 1 Arc-Second Global dataset, which provides elevation data at approximately 30-meter spatial resolution. The SRTM tiles covering the Senegalese territory were downloaded from the CGIAR-CSI repository and mosaicked to construct a seamless digital elevation model (DEM) of the study area. To minimize noise and data artifacts, a mean filter was applied, and known voids were corrected using interpolation techniques. All DEM data were reprojected to the WGS 84 / UTM Zone 28N coordinate system to ensure spatial consistency with other environmental datasets.

This elevation model served as the base layer for extracting first- and second-order terrain attributes, including slope, aspect, and curvature, which are essential for hydrological modeling. These derivatives were computed using finite-difference approximations over a regular grid and stored as raster layers for further analysis. Slope was particularly important for assessing runoff dynamics, while curvature was used as a proxy for terrain convergence and divergence. These terrain metrics provided the foundation for evaluating surface water redistribution potential across the landscape and served as key inputs for the subsequent computation of the Runoff Potential Index (RPI).

Soil Data

Soil information was obtained from SoilGrids, a global soil information system developed by ISRIC–World Soil Information. SoilGrids uses machine learning to generate continuous maps of soil attributes at 250-meter spatial resolution and multiple standard depths (15 cm, 30 cm, and 100 cm). For this study, all three depth layers were used to extract key variables: sand, silt, clay percentages; soil organic carbon (g/kg); pH; bulk density (kg/m³); cation-exchange capacity (cmol/kg); and volumetric water content. These properties were resampled and aligned to the modeling grid, ensuring consistency with climate and topographic data.

Soil texture classes were derived using USDA classification schemes to capture spatial heterogeneity in hydraulic conductivity and field capacity. These attributes were critical for simulating water retention behavior and estimating drought vulnerability across upland and lowland zones, providing comprehensive representation of soil physical and chemical conditions as primary inputs for the CERES-Rice simulations.

Climate Data

Meteorological variables were sourced from the NASA POWER (Prediction Of Worldwide Energy Resource) database, which provides globally available, satellite-derived weather data specifically optimized for agricultural and agroclimatic applications. This dataset integrates satellite observations with ground station data and assimilated outputs to generate consistent time series at a spatial resolution of approximately 0.5 degrees (50 km) and daily temporal resolution.

The following variables were extracted for each georeferenced location across the study region: minimum and maximum temperature (°C), solar radiation (MJ/m^2/day), wind speed (m/s), relative humidity (%), and precipitation (mm/day). These variables were selected to meet the input requirements of the CERES-Rice model within the DSSAT platform, which relies on accurate daily weather inputs to simulate crop growth and water stress dynamics.

NASA POWER data have been extensively validated in the context of crop modeling and yield estimation in tropical regions, and have demonstrated reliable performance in the absence of dense ground-based weather networks. In this study, the dataset enabled consistent temporal coverage over the 2000–2019 simulation period and facilitated the spatial integration of weather patterns with soil and topographic datasets. This climate information was used to drive daily evapotranspiration and soil moisture calculations, forming the core of the drought stress simulation framework.

Runoff Potential Index (RPI) Computation

To characterize terrain-driven water redistribution, a novel curvature-based metric, Runoff Potential Index (RPI), was computed from digital elevation data. The RPI quantifies the combined effects of local concavity and slope magnitude to identify areas with higher water accumulation potential (e.g., lowland depressions) versus zones more prone to surface runoff (e.g., convex uplands). Unlike conventional indices such as the Topographic Wetness Index (TWI), which rely heavily on slope and often exhibit numerical instability in low-relief terrains, RPI incorporates second-order terrain information for enhanced morphological discrimination.

The RPI formulation integrates local terrain curvature with slope steepness through the mathematical framework:

$$\mathrm{RPI}(x,y) = \frac{\nabla^2 z}{|\nabla z| + \varepsilon} \quad \text{where} \quad \nabla^2 z = \frac{\partial^2 z}{\partial x^2} + \frac{\partial^2 z}{\partial y^2}, \quad |\nabla z| = \sqrt{\left(\frac{\partial z}{\partial x}\right)^2 + \left(\frac{\partial z}{\partial y}\right)^2}, \quad \varepsilon = 10^{-12} \tag{1}$$

The terrain elevation function $z = z(x,y)$ defines the topographic surface, while $\nabla^2 z$ captures morphological concavity (positive values) or convexity (negative values). The regularization parameter ε ensures computational stability in flat regions where $|\nabla z| \to 0$. This formulation yields a physically interpretable metric where positive RPI values indicate convergent flow patterns characteristic of water-retaining lowlands, negative values represent divergent flow typical of runoff-prone uplands, and values near zero correspond to neutral terrain with balanced water redistribution.

Upland-Lowland Classification Based on Runoff Behavior

The classification of agricultural landscapes into upland and lowland zones represents a fundamental approach in hydrology and geomorphology, with multiple definitions existing across different scientific disciplines. In geomorphological contexts, uplands are traditionally defined as elevated terrain with steep slopes and high drainage density[53,54], while lowlands correspond to flat, low-lying areas associated with alluvial plains and stream terraces[55,56]. Agricultural perspectives often emphasize soil drainage characteristics, where uplands exhibit well-drained soils with rapid water movement, and lowlands are associated with poorly drained, waterlogged conditions[57,58]. However, these conventional definitions inadequately capture the morphological controls on surface water redistribution that are critical for drought vulnerability assessment[21,59].

For this study, upland areas are specifically defined as topographic positions characterized by convex morphology that promotes rapid surface runoff and limited water retention, where terrain curvature induces flow divergence away from the local area. Lowland areas represent concave terrain features such as depressions, valleys, and convergence zones where surface water accumulates and infiltration is enhanced, providing increased drought resilience through improved soil moisture retention.

The RPI directly quantifies this morphological distinction through its curvature-based formulation, where negative values correspond to upland characteristics (divergent flow patterns) and positive values indicate lowland behavior (convergent flow patterns). The classification employs percentile thresholds to systematically differentiate these hydrological zones: upland areas are identified using the 20th percentile threshold (RPI < 0.2 percentile), lowland areas correspond to the 80th percentile threshold (RPI > 0.8 percentile), while intermediate values represent neutral terrain with balanced water redistribution patterns (Figure 2). This approach provides robust morphological discrimination across diverse terrain conditions, enabling systematic identification of drought-vulnerable versus resilient agricultural zones based on inherent landscape structure.

Computational Implementation

RPI values were calculated for each grid cell using a custom computational framework developed for this study: *The Runoff Potential Index: Upland–Lowland Differentiation Toolbox (v1.0.0)*. This MATLAB-based implementation incorporates a 3D physics-based simulation engine for surface water dynamics, enabling real-time visualization of flow behavior under variable terrain scenarios. The toolbox supports automated water divergence computation supporting the interpretation of RPI through optimized finite-difference approximations and provides exportable analytical outputs for scientific analysis and presentation.

The computational framework implements spatial filtering algorithms to minimize noise artifacts in satellite-derived elevation data while preserving critical microtopographic variations essential for accurate hydrological characterization. Designed specifically for rainfed agricultural systems, the toolbox enables precision identification of drought-vulnerable uplands and water-retentive lowlands, systematically overcoming the numerical limitations of slope-dependent indices in low-gradient landscapes.

The mathematical framework in Equation 1, combined with the robust computational implementation, provides systematic quantification of terrain-induced hydrological behavior across diverse morphological conditions, enabling scalable identification of drought-vulnerable versus resilient zones based on inherent landscape structure without reliance on ground-based instrumentation.

Mechanistic Crop Model

The CERES-Rice model within the DSSAT framework was selected over alternative rice simulation models (ORYZA, APSIM, AquaCrop) based on two critical factors: (1) availability of validated genetic coefficients for West African rice varieties, specifically NERICA cultivars extensively calibrated by Gérardeaux et al.[60] and optimized by Correa et al.[61] under Senegalese conditions; and (2) robust integration capabilities with satellite-derived environmental datasets, particularly its capacity to utilize multi-layer soil profiles from SoilGrids at three distinct depths (15 cm, 30 cm, 100 cm), unlike alternative models that typically operate with single-layer soil representations, enabling more realistic representation of soil water dynamics essential for regional-scale drought assessment in data-scarce environments.

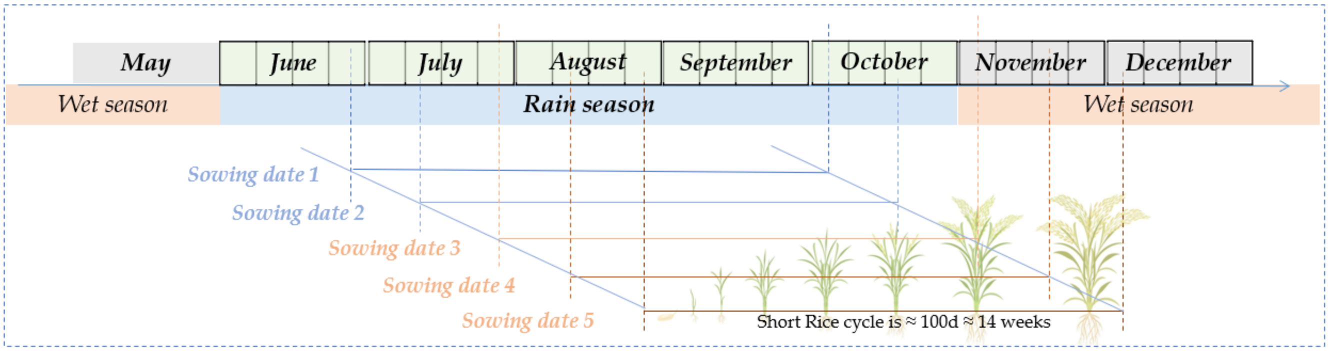

Figure 11. Temporal distribution of the five sowing date scenarios used in simulations. Each window is spaced by 15 days, aligned with the rainy season in southern Senegal. A short-cycle rice cultivar (≈ 100 days) was simulated for each planting date.

CERES-Rice is a process-based, daily time-step crop model that simulates growth, development, and yield of rice as a function of genotype, weather, soil conditions, and management practices. It has been extensively implemented and is widely used for evaluating crop performance under water-limited conditions.

Soil hydraulic properties and climate inputs were derived from satellite-based datasets (as described in Section 2), while cultivar-specific genetic coefficients were calibrated using field trial data from previous studies in Senegal. Phenological development is modeled through thermal time accumulation, allowing the model to capture temperature-driven growth stage transitions. The simulations conducted in this study focus exclusively on water stress, assuming optimal nutrient conditions and no biotic constraints.

Simulation Scenarios

A total of 506 georeferenced locations were selected to provide comprehensive spatial coverage across the study region, representing approximately one sampling point per 140 km² across the 70,000 km² study area. This sampling density ensures adequate representation of diverse agroecological conditions and enables subsequent terrain-based analysis using RPI spatial aggregation with 2.5-km search radius, while maintaining computational efficiency for the extensive simulation framework (50,600 total simulations across 20 years and 5 sowing dates).

Simulations were conducted across five sowing dates at 15-day intervals (late June to late August) to capture the transition from water-sufficient to water-limited growing conditions. Early sowing dates (S1-S2) ensure the complete 100-day rice cycle occurs within peak rainfall, while late dates (S4-S5) expose grain filling to dry season onset, enabling quantification of drought stress gradients and identification of optimal planting windows for climate adaptation strategies[60].

Simulations spanned 20 years (2000–2019) encompassing representative regional climatic variability. Each simulation was location-specific, incorporating terrain-derived soil hydrological attributes and satellite-based meteorological data, as described in Section 2. Figure 11 illustrates the temporal distribution of the five sowing scenarios relative to the rainy season and the approximate 100-day crop cycle.

Drought Stress Characterization

In the context of drought analysis, the model calculates crop water requirements based on potential evapotranspiration (ET), estimated using the FAO Penman-Monteith method. Daily water balance is computed by accounting for precipitation, deep percolation, and ET. When the crop's water demand exceeds the plant-available soil water, the model accounts for stress functions that reduce photosynthesis, leaf expansion, and biomass accumulation, ultimately affecting yield.

The CERES-Rice model simulates drought stress by comparing daily crop water demand with plant-available soil water content throughout the growing season. Water demand is determined by potential evapotranspiration (ET), while soil moisture dynamics are updated daily through a water balance model that incorporates precipitation, infiltration, drainage, and evapotranspiration losses. Water stress occurs when the ratio of available soil water to ET, defined as the water supply-to-demand ratio, falls below unity, resulting in reductions in carbon assimilation and growth processes.

To assess the impact of drought on crop development, the stress index was computed across seven individual phenological stages (Germination, Stem Growth, Panicle Initiation, Panicle Extension, Flowering, Grain Filling, and Maturation), which were subsequently grouped into four key developmental phases: Early Growth (germination and stem growth), Panicle Phase (panicle initiation and extension), Flowering (anthesis), and Grain & Maturation (grain filling and maturation). These phases correspond to distinct physiological processes with differing sensitivity to water stress. For each simulation, drought intensity was quantified as the average daily stress index during each stage, with values ranging from 0 (no stress) to 1 (maximum stress).

The onset and duration of phenological stages were determined dynamically based on thermal time accumulation, allowing the model to capture inter-annual and sowing-date variability in crop development. This approach enables stage-specific assessment of drought impact, which is essential for identifying critical windows of vulnerability in rainfed rice systems.

Target Population of Environments (TPE)

To identify representative drought environments across the study region, the full set of crop simulations was analyzed using a clustering approach based on stage-specific drought stress patterns. Each simulation produced four stress intensity values—one for each key phenological stage (tillering, panicle initiation, anthesis, and grain filling)—resulting in a four-dimensional feature vector characterizing the temporal distribution of water stress.

To classify these environments, an unsupervised clustering algorithm was applied to the phenological stress feature space. The optimal number of clusters was determined using the Silhouette Coefficient and Davies–Bouldin Index, ensuring both inter-cluster separation and intra-cluster consistency. Clustering was performed independently for each year to preserve inter-annual variability and capture year-specific drought patterns.

Each resulting cluster represents a distinct drought environment characterized by a specific temporal stress signature. These drought-driven TPEs were then used to analyze yield stability, sowing date interactions, and spatial drought risk patterns, providing a robust framework for environmental classification in rainfed rice systems.

References

1. United Nations Office for Disaster Risk Reduction. Gar special report on drought 2021. Tech. Rep., United Nations Office for Disaster Risk Reduction, Geneva, Switzerland (2021).
2. United Nations Convention to Combat Desertification, Economics of Land Degradation Initiative & United Nations University Institute for Water, Environment and Health. Economics of drought: Investing in nature-based solutions for drought resilience – proaction pays. Tech. Rep., United Nations Convention to Combat Desertification, Bonn, Germany (2024).
3. IPCC. Climate change 2023: Synthesis report. contribution of working groups i, ii and iii to the sixth assessment report of the intergovernmental panel on climate change. Tech. Rep., Intergovernmental Panel on Climate Change, Geneva, Switzerland (2023). DOI: 10.59327/IPCC/AR6-9789291691647.
4. Gutaker, R. M. *et al.* Genomic history and ecology of the geographic spread of rice. *Nat. Plants* **6**, 492 – 502, DOI: 10.1038/s41477-020-0659-6 (2020). Cited by: 158; All Open Access, Green Open Access.
5. Gross, B. L. & Zhao, Z. Archaeological and genetic insights into the origins of domesticated rice. *Proc. Natl. Acad. Sci. United States Am.* **111**, 6190 – 6197, DOI: 10.1073/pnas.1308942110 (2014). Cited by: 276; All Open Access, Green Open Access.
6. Muthayya, S., Sugimoto, J. D., Montgomery, S. & Maberly, G. F. An overview of global rice production, supply, trade, and consumption. *Annals New York Acad. Sci.* **1324**, 7 – 14, DOI: 10.1111/nyas.12540 (2014). Cited by: 1084.
7. Feng, X., Porporato, A. & Rodriguez-Iturbe, I. Changes in rainfall seasonality in the tropics. *Nat. Clim. Chang.* **3**, 811 – 815, DOI: 10.1038/nclimate1907 (2013). Cited by: 476.
8. Lafitte, H., Yongsheng, G., Yan, S. & Li, Z.-K. Whole plant responses, key processes, and adaptation to drought stress: The case of rice. *J. Exp. Bot.* **58**, 169 – 175, DOI: 10.1093/jxb/erl101 (2007). Cited by: 209; All Open Access, Bronze Open Access, Green Open Access.
9. Oyebamiji, Y. O., Shamsudin, N. A. A., Asmuni, M. I. & Adebola, L. A. Drought impacts and the tolerance mechanisms in rice (oryza sativa l.): A review. *Egypt. J. Agron.* **44**, 97 – 115, DOI: 10.21608/AGRO.2022.140551.1321 (2022). Cited by: 3; All Open Access, Bronze Open Access.
10. Rasheed, A. *et al.* A critical review on the improvement of drought stress tolerance in rice (oryza sativa l.). *Notulae Bot. Horti Agrobot. Cluj-Napoca* **48**, 1756 – 1788, DOI: 10.15835/48412128 (2020). Cited by: 44.
11. Di Paola, A., Valentini, R. & Santini, M. An overview of available crop growth and yield models for studies and assessments in agriculture. *JOURNAL OF THE SCIENCE OF FOOD AND AGRICULTURE* **96**, 709–714, DOI: 10.1002/jsfa.7359 (2016).
12. Hoogenboom, G., White, J. W. & Messina, C. D. From genome to crop: integration through simulation modeling. *Field Crop. Res.* **90**, 145–163, DOI: https://doi.org/10.1016/j.fcr.2004.07.014 (2004). Linking Functional Genomics with Physiology for Global Change Research.
13. Chapagain, R. *et al.* Decomposing crop model uncertainty: A systematic review. *Field Crop. Res.* **279**, DOI: 10.1016/j.fcr.2022.108448 (2022). Cited by: 41.

14. Stock, M., Pieters, O., De Swaef, T. & Wyffels, F. Plant science in the age of simulation intelligence. *FRONTIERS IN PLANT SCIENCE* **14**, DOI: 10.3389/fpls.2023.1299208 (2024).

15. Balsamo, G. *et al.* Satellite and in situ observations for advancing global earth surface modelling: A review. *Remote. Sens.* **10**, DOI: 10.3390/rs10122038 (2018). Cited by: 118; All Open Access, Gold Open Access, Green Open Access.

16. Khalfallah, M., Martinez, A., Blade, C., Ludwig, T. & Ghodous, P. Satellite reference databases scope and data organization: A literature review. *Comput. Ind.* **149**, DOI: 10.1016/j.compind.2023.103913 (2023). Cited by: 2.

17. Li, Q. *et al.* Topography significantly influencing low flows in snow-dominated watersheds. *Hydrol. Earth Syst. Sci.* **22**, 1947–1956, DOI: 10.5194/hess-22-1947-2018 (2018).

18. Amatulli, G. *et al.* A suite of global, cross-scale topographic variables for environmental and biodiversity modeling. *Sci. Data* **5**, 180040, DOI: 10.1038/sdata.2018.40 (2018).

19. Moore, I. D., Grayson, R. B. & Ladson, A. R. Digital terrain modelling: a review of hydrological, geomorphological, and biological applications. *Hydrol. Process.* **5**, 3–30, DOI: 10.1002/hyp.3360050103 (1991).

20. Wilson, J. P. & Gallant, J. C. *Terrain Analysis: Principles and Applications* (John Wiley & Sons, New York, 2000).

21. Beven, K. J. & Kirkby, M. J. A physically based, variable contributing area model of basin hydrology. *Hydrol. Sci. Bull.* **24**, 43–69, DOI: 10.1080/02626667909491834 (1979).

22. Schmidt, S., Alewell, C. & Meusburger, K. Modification of the rusle slope length and steepness factor (ls-factor) based on rainfall experiments at steep alpine grasslands. *MethodsX* **6**, 219–229, DOI: 10.1016/j.mex.2019.01.004 (2019).

23. Hjerdt, K. N., McDonnell, J. J., Seibert, J. & Rodhe, A. A new topographic index to quantify downslope controls on local drainage. *Water Resour. Res.* **40**, W05602, DOI: 10.1029/2004WR003130 (2004).

24. Zevenbergen, L. W. & Thorne, C. R. Quantitative analysis of land surface topography. *Earth Surf. Process. Landforms* **12**, 47–56, DOI: 10.1002/esp.3290120107 (1987).

25. Florinsky, I. V. *An Illustrated Introduction to General Geomorphometry*, vol. 41 (SAGE Publications, 2017).

26. Passalacqua, P., Do Trung, T., Foufoula-Georgiou, E., Sapiro, G. & Dietrich, W. E. A geometric framework for channel network extraction from lidar: Nonlinear diffusion and geodesic paths. *J. Geophys. Res. Earth Surf.* **115**, F01002, DOI: 10.1029/2009JF001254 (2010).

27. Mattivi, P., Franci, F., Lambertini, A. & Bitelli, G. Twi computation: a comparison of different open source giss. *Open Geospatial Data, Softw. Standards* **4**, DOI: 10.1186/s40965-019-0066-y (2019).

28. McKee, T. B., Doesken, N. J. & Kleist, J. The relationship of drought frequency and duration to time scales. *Proc. 8th Conf. on Appl. Climatol.* 179–183 (1993).

29. Van Rooy, M. P. A rainfall anomaly index independent of time and space. *Notos* **14**, 43–48 (1965).

30. Kogan, F. N. Application of vegetation index and brightness temperature for drought detection. *Adv. Space Res.* **15**, 91–100, DOI: 10.1016/0273-1177(95)00079-T (1995).

31. Kogan, F. N. Global drought watch from space. *Bull. Am. Meteorol. Soc.* **78**, 621–636, DOI: 10.1175/1520-0477(1997)078<0621:GDWFS>2.0.CO;2 (1997).

32. Zhang, D. & Jia, G. Spatial-temporal variation of soil moisture and its relationship with meteorological factors over the tibetan plateau. *J. Geophys. Res. Atmospheres* **118**, 1835–1844, DOI: 10.1002/jgrd.50162 (2013).

33. Riley, S. J., DeGloria, S. D. & Elliot, R. A terrain ruggedness index that quantifies topographic heterogeneity. *Intermountain J. Sci.* **5**, 23–27 (1999).

34. Daly, C. *et al.* Physiographically sensitive mapping of climatological temperature and precipitation across the conterminous united states. *Int. J. Climatol.* **28**, 2031–2064, DOI: 10.1002/joc.1688 (2008).

35. Palmer, W. C. Meteorological drought. *U.S. Weather. Bureau Res. Pap.* **45**, 58 (1965).

36. Xu, H. Modification of normalised difference water index (ndwi) to enhance open water features in remotely sensed imagery. *Int. J. Remote. Sens.* **27**, 3025–3033, DOI: 10.1080/01431160600589179 (2006).

37. Bastiaanssen, W. G. M., Menenti, M., Feddes, R. A. & Holtslag, A. A. M. A remote sensing surface energy balance algorithm for land (sebal). 1. formulation. *J. Hydrol.* **212**, 198–212, DOI: 10.1016/S0022-1694(98)00253-4 (1998).

38. Ishihara, T. & Kobatake, S. Runoff model for flood forecasting. *Bull. Disaster Prev. Res. Inst.* **29**, 27–43 (1979).

39. National Research Center for Disaster Prevention. Tank model for runoff analysis. Tech. Rep., NRCDP, Japan (1970).

40. Bergström, S. Development and application of a conceptual runoff model for scandinavian catchments. *SMHI Reports RHO* **7**, 134 (1976).

41. Burnash, R. J. C., Ferral, R. L. & McGuire, R. A. A generalized streamflow simulation system: Conceptual modeling for digital computers. Tech. Rep., National Weather Service and State of California Department of Water Resources (1973).

42. Nielsen, S. A. & Hansen, E. Numerical simulation of the rainfall-runoff process on a daily basis. *Nord. Hydrol.* **12**, 217–238 (1981).

43. Boughton, W. C. The australian water balance model. *Environ. Model. & Softw.* **19**, 943–956 (2004).

44. Jones, J. *et al.* The dssat cropping system model. *Eur. J. Agron.* **18**, 235–265, DOI: 10.1016/S1161-0301(02)00107-7 (2003).

45. Breiman, L. Random forests. *Mach. Learn.* **45**, 5–32, DOI: 10.1023/A:1010933404324 (2001).

46. White, J. W., Hoogenboom, G., Stackhouse, P. W. & Hoell, J. M. Evaluation of nasa satellite- and assimilation model-derived long-term daily temperature data over the continental us. *Agric. For. Meteorol.* **148**, 1574–1584, DOI: https://doi.org/10.1016/j.agrformet.2008.05.017 (2008).

47. DSSAT Foundation. Nasa power sse weather data for dssat applications. (2024). Accessed: 2024.

48. White, J. W., Hoogenboom, G., Wilkens, P. W., Stackhouse Jr., P. W. & Hoel, J. M. Evaluation of satellite-based, modeled-derived daily solar radiation data for the continental united states. *Agron. J.* **103**, 1242 – 1251, DOI: 10.2134/agronj2011.0038 (2011). Cited by: 100.

49. Sagna, P. *et al.* Climate change and water resources in west africa: A case study of ivory coast, benin, burkina faso, and senegal. In *Climate Change and Water Resources in Africa* (2016).

50. Boonjung, H. & Fukai, S. Effects of soil water deficit at different growth stages on rice growth and yield under upland conditions. 2. phenology, biomass production and yield. *Field Crop. Res.* **48**, 47–55, DOI: 10.1016/0378-4290(96)00039-1 (1996).

51. Yang, X., Wang, B., Chen, L., Li, P. & Cao, C. The different influences of drought stress at the flowering stage on rice physiological traits, grain yield, and quality. *Sci. Reports* **9**, 3742, DOI: 10.1038/s41598-019-40161-0 (2019).

52. Jongdee, B., Fukai, S. & Cooper, M. Leaf water potential and osmotic adjustment as physiological traits to improve drought tolerance in rice. *Field Crop. Res.* **76**, 153–163, DOI: 10.1016/S0378-4290(02)00036-9 (2002).

53. Strahler, A. N. Quantitative analysis of watershed geomorphology. *Transactions Am. Geophys. Union* **38**, 913–920, DOI: 10.1029/TR038i006p00913 (1957).

54. Gregory, K. J. & Walling, D. E. *Drainage Basin Form and Process: A Geomorphological Approach* (Edward Arnold, London, 1973).

55. Hudson, P. F. *Flooding and Management of Large Fluvial Lowlands: A Global Environmental Perspective* (Cambridge University Press, Cambridge, 2021).

56. Thorne, C. R. Geomorphic analysis of large alluvial rivers. *Geomorphology* **44**, 203–219, DOI: 10.1016/S0169-555X(01)00175-1 (2002).

57. Soil Survey Division Staff. Soil survey manual. Tech. Rep. Agriculture Handbook 18, USDA-SCS, Washington, DC (1993).

58. Schaetzl, R. J. & Anderson, S. *Soils: Genesis and Geomorphology* (Cambridge University Press, Cambridge, 2005).

59. Sørensen, R., Zinko, U. & Seibert, J. On the calculation of the topographic wetness index: evaluation of different methods based on field observations. *Hydrol. Earth Syst. Sci.* **10**, 101–112, DOI: 10.5194/hess-10-101-2006 (2006).

60. Gérardeaux, E. *et al.* Adapting rainfed rice to climate change: a case study in senegal. *Agron. for Sustain. Dev.* **41**, 57, DOI: 10.1007/s13593-021-00710-2 (2021).

61. Correa, E. S., Calderon, F. C. & Colorado, J. D. Ai-driven remote sensing for environmental characterization and rice crop modeling in water-limited regions. DOI: 10.21203/rs.3.rs-6440110/v1 (2025).

Acknowledgements

The author expresses deep gratitude to the UMR-AGAP Institute (Genetic Improvement and Adaptation of Mediterranean and Tropical Plants) and the School of Engineering at Javeriana University for their support and for granting access to research facilities. The author also thanks CIRAD for providing the Ph.D. scholarship that enabled this work.

Sincere appreciation is extended to Julian Colorado, Myriam Adam, Francisco Calderon, and Maria Camila Rebolledo for their contributions in formulating the research project and supporting the application of crop models.

Special acknowledgment is given to Edward Gerardeaux for providing crop parameters and observational data for the rice variety NERICA 4, as detailed in Gerardeaux et al. (2021), and to Alfredo Taboada for his deep insights into geomorphology. The author acknowledges valuable feedback received during the 2024 doctoral committee presentations.

Author contributions statement

E.S.C. (Edgar S. Correa) was responsible for: Conceptualization, Methodology, Software, Validation, Formal Analysis, Investigation, Data Curation, Writing—Original Draft, Writing—Review and Editing, and Visualization.

Funding

This research was funded by the Agropolis Fondation through the CropModAdapt project (Contract No. 2201-026) and the ClimBeR initiative - France-CGIAR action plan on climate change (ICARDA Agreement No. 200303).

Data and Code Availability

All source code used to compute and visualize the Runoff Potential Index (RPI), including the physics-based water redistribution simulations, is publicly available at the following repositories:

RPI Toolbox:

- The Runoff Potential Index: Upland-lowland differentiation. MATLAB Central File Exchange. Updated: June 11, 2025
- GitHub Repository: Drought-stress-crop-scale

Released under the Apache License, Version 2.0 (Apache-2.0).

Crop Growth Modelling Data and Scripts:

- Mendeley Data (DOI: 10.17632/fwp748vfkx.1). Published: January 20, 2025
- GitHub Repository: Crop-Growth-Modelling

Released under the Creative Commons Attribution 4.0 International License (CC BY 4.0).

Competing Interests

The author declares no competing interests.